Manuscript prepared for Atmos. Chem. Phys. Discuss.
with version 2014/05/30 6.91 Copernicus papers of the LaTeX class copernicus.cls.
Date: 20 January 2016

Aerosol size distribution seasonal characteristics measured in Tiksi, Russian Arctic

E. Asmi[1], V. Kondratyev[1,2], D. Brus[1], T. Laurila[1], H. Lihavainen[1], J. Backman[1], V. Vakkari[1], M. Aurela[1], J. Hatakka[1], Y. Viisanen[1], T. Uttal[3], V. Ivakhov[4], and A. Makshtas[5]

[1]Atmospheric Composition Research, Finnish Meteorological Institute, Helsinki, Finland
[2]Yakutian service for hydrometeorology and environmental monitoring, Tiksi branch, Russia
[3]National Oceanic and Atmospheric Administration, Boulder, USA
[4]Voeikov Main Geophysical Observatory, St. Petersburg, Russia
[5]Arctic and Antarctic Research Institute, St. Petersburg, Russia.

Correspondence to: E. Asmi
(eija.asmi@fmi.fi)

Abstract

Four years of continuous aerosol number size distribution measurements from an Arctic Climate Observatory in Tiksi Russia are analyzed. Tiksi is located in a region where in-situ information on aerosol particle properties has not been previously available. Particle size distributions were measured with a differential mobility particle sizer (at diameter range 7–500 nm) and with an aerodynamic particle sizer (at diameter range 0.5–10 μm). Source region effects on particle modal features, and number and mass concentrations are presented for different seasons. The monthly median total aerosol number concentration in Tiksi ranges from 184 cm^{-3} in November to 724 cm^{-3} in July with a local maximum in March of 481 cm^{-3}. The total mass concentration has a distinct maximum in February–March of 1.72–2.38 $\mu\text{g m}^{-3}$ and two minimums in June of 0.42 $\mu\text{g m}^{-3}$ and in September–October of 0.36–0.57 $\mu\text{g m}^{-3}$. These seasonal cycles in number and mass concentrations are related to isolated processes and phenomena such as Arctic haze in early spring which increases accumulation and coarse mode numbers, and secondary particle formation in spring and summer which affects the nucleation and Aitken mode particle concentrations. Secondary particle formation was frequently observed in Tiksi and was shown to be slightly favored in marine, in comparison to continental, air flows. Particle formation rates were the highest in spring while the particle growth rates were peaking in summer. These results suggest two different origins for secondary particles, anthropogenic pollution being the important source in spring and biogenic emissions in summer. The impact of temperature dependent natural emissions on aerosol and cloud condensation nuclei numbers was significant: increase of both the particle mass and the CCN number with temperature was found to be higher than in any previous study done over the boreal forests region. In addition to the precursor emissions of biogenic volatile organic compounds, the frequent Siberian forest fires, although far away are suggested to play a role in Arctic aerosol composition during the warmest months. Five fire events were isolated based on clustering analysis and particle mass and cloud condensation nuclei number were shown to be somewhat affected by these events. In addition, during calm and cold months aerosol concentrations were occasionally increased

by local aerosol sources in trapping inversions. These results provide valuable information on inter-annual cycles and sources of Arctic aerosols.

1 Introduction

The Arctic and northern boreal regions of Eurasia are changing rapidly as a consequence of increased human activities (Richter-Menge et al., 2006; Bond et al., 2013). Aerosol particles are one of the major climate forcers in the Arctic; they reflect and absorb the incoming solar radiation, modify the properties of clouds and affect the surface albedo. Shindell and Faluvegi (2009) suggested that over two thirds of the observed Arctic surface temperature increase during the last decades is attributed to changes in concentrations of sulphate and black carbon (BC) aerosols.

Aerosol particles on snow and ice-covered regions have specific climate impacts and feedback processes. Recent experimental evidence indicates that in pristine polar regions the aerosol-cloud feedback can be extremely sensitive to aerosol numbers. It was shown that even a small increase in particle number leads to an increased cloud droplet number concentration thus affecting the cloud radiative properties but also decreasing the cloud maximum supersaturation (Asmi et al., 2012). The Arctic clouds, contrary to those occurring at lower latitudes, can enhance overall warming of the surface (Walsh and Chapman, 1998; Mauritsen et al., 2011). To understand these processes, information on aerosol sizes is of particular interest, however, only a few long-term studies of aerosol number and size distributions from the Arctic locations exist (Bodhaine, 1989; Tunved et al., 2013). These have suggested a rather clear seasonal cycle of increased particle number and mass in early spring as a consequence of the Arctic Haze phenomena (Mitchell, 1957). Currently, the commonly used global and chemical transport models consistently fail in predicting the Arctic aerosol seasonal cycles, and also encounter problems in capturing the composition and quantities of polar aerosols (Bourgeois and Bey, 2011; Liu et al., 2012; Bond et al., 2013; Eckhardt et al., 2015). Several studies suggest that this can be attributed to problems in treatment of the aerosol transport in models, and in particular in wet scavenging processes (e.g., Liu et al., 2012). Some recent studies also indicate that a number of sources have been neglected (Hienola et al., 2013; Stohl et al., 2013; Stock et al., 2014). Eckhardt et al. (2015) compared the absorbing aerosol concentration measured in Tiksi, Russia with several models results and found a major discrepancy throughout most of the year where the measured annual average concentration exceeded that of modeled by 3-fold. This suggests a significant underestimation of black carbon concentration in emission inventories in Russia, but also highlights the need of more detailed data from this region.

South of the Arctic on the Eurasian side is the vast Siberian region from which knowledge of aerosol properties is particularly limited. Recently, some studies documenting interannual variability of aerosol distributions from central Siberia were published highlighting the importance of emissions of biogenic volatile organic compounds (BVOCs) on aerosol number and mass distributions in Siberian boreal forests (Heintzenberg et al., 2008, 2011; Chi et al., 2013). The impact of BVOC emissions on aerosol numbers and mass, and the temperature related feedback connected with these emissions, is suggested by previous studies from other boreal regions (Tunved et al., 2006; Asmi et al., 2011; Paasonen et al., 2013); however, the relative importance of biogenic emissions for aerosols in the current and future warming Arctic is still an open question.

In this work, to fill these observational data gaps, we present long-term, high-quality observations from Arctic Siberia by introducing four years of continuous aerosol number size distribution observations from the Tiksi Hydrometeorological Observatory. We will quantify aerosol modal features, number and mass concentrations and analyze their temporal evolution in terms of source region controls and local weather parameters. Our goal is to assess the effects of BVOC emissions from Siberian boreal regions and wild fire emissions on the aerosol particle size distributions at Tiksi, as well as to describe the build-up of the Arctic haze in the region. Analysis of the nucleation mode aerosols indicates how secondary sources contribute significantly to the aerosol particle concentrations under different conditions in the Arctic.

2 Methods

2.1 Site description

History and a general overview of Tiksi International Hydrometeorological Observatory is fully described in Uttal et al. (2013). Tiksi meteorological observatory in northern Siberia 71° 36′ N; 128° 53′ E) on the shore of the Laptev Sea has been operating since 1930s. As an International Polar Year (IPY) 2007–2008 activity, the observatory was further upgraded and joined in the network of the International Arctic Systems for Observing the Atmosphere (IASOA, www.IASOA.org). The Tiksi observatory is run in collaboration between NOAA (National Oceanic and Atmospheric Administration), Roshydromet AARI (Arctic and Antarctic Research Institute) and MGO (The Voeikov Main Geophysical Observatory) units, Yakutian service for hydrometeorology and environmental monitoring, and the FMI (Finnish Meteorological Institute). FMI activities in Tiksi were initiated in summer 2010 and include aerosol number size distribution measurements presented here.

The city of Tiksi is on the Lena river delta with current population of about 5000 inhabitants. Meteorological observatory is located 5 km further down to south-west from the city, separated by a hill, and is about 500 m distance from the coast of the Laptev sea (Fig. 1 and Fig. S1 in supplement). Airport of Tiksi is further up north from the city and the station. The site is far north of the treeline and is surrounded by low tundra vegetation and a line of mountains in the south.

2.2 Measurements

Measurements of aerosol size distributions, along with many other atmospheric parameters (for these, see Uttal et al. (2013)), were started in July 5, 2010. Aerosol number size distribution from 7 to 500 nm (later on from 3 to 800 nm) is measured with a twin-Differential Mobility Particle Sizer (DMPS) system and the distribution up from 500 nm with an Aerodynamic Particle Sizer (APS model 3321, TSI Inc., USA). For further description of the instruments, see section 2.2.1. Time resolution of the DMPS measurements was set to 10 min and APS to 5 min.

Both of the instruments are attached to a stainless steel inlet tube with outer diameter, O.D.=16 mm and inner diameter, I.D.=12 mm. The tube is fixed just above the instrument rack and extending 2 m above the roof of the building (i.e. 6.5 m above the ground level). The APS inlet is direct from the roof, with a total length of 2.5 m. The DMPS inlet length is 4–5 m, and the theoretical diffusional losses for laminar tube flow during the particle transport are taken into account in the data inversion (Hinds, 1999).

The inlet tube is equipped with an inlet head of a fixed cut-off size of 10 μm (BGI Inc, USA). The head also protects the instruments from snow, rain and soil contaminants. Flow through the inlet is kept at a constant 1 m^3 h^{-1} with an additional compensating flow, regulated depending on the total flow of all instruments. For example, when an aethalometer with a flow-rate of 5 liters per minute (LPM) was added on line with the DMPS and APS in August 2010, the compensating flow was reduced from 10 to 5 LPM. Heating (self-regulating) and isolation were added on the inlet tube in summer 2012, after two winters of relatively poor data coverage due to icing problems.

The flows and proper operation of all the instruments are fully checked twice per year during the station maintenance visits. Additionally, the automated flow, temperature and pressure sensors allow the control of instruments and data over the span of the year. The station staff is trained to solve problems which might occur unexpectedly and they are also in charge of the regular maintenance done weekly.

Data are transferred real-time to AARI via satellite connection and daily to NOAA and FMI servers, and quality checked weekly.

2.2.1 Size distributions

The twin-Differential Mobility Particle Sizer (DMPS) system used in Tiksi since 2010, as well as our data inversion procedure, are thoroughly described in Wiedensohler et al. (2012) and here only a brief summary is given.

The twin-DMPS consists of two identical DMPS systems: one equipped with a short Vienna-type DMA to measure particle sizes from 7 to 115 nm and one with a medium-long Vienna-type DMA to measure particle sizes from 15 to 500 nm. Both use a condensation particle counter (CPC model 3772, TSI Inc., USA) as a particle detector, with the adjusted temperature difference between the CPC saturator and condenser of 23 °C and calibrated to a cut-off size of 7 nm using silver nanoparticles. DMPS sheath flows are controlled by a blower (Ametek, USA) and regulated with a PID-controller. Aerosol flow rate of 1 LPM and sheath flow rate of 6 LPM are used. The size range of DMPS measurements was extended up to 800 nm in May 15, 2012. Further extension of the measurement size range down to 3 nm was done in July 3, 2013, when the original CPC model 3772 was replaced with a CPC model 3776 (TSI Inc., USA) . The CPC 3772 was then installed to measure the particle total number concentration. Flows of the short-DMPS system after this are 1.5 and 9 LPM, for aerosol and sheath respectively. Dryer is not used in front of the instruments since the sample air RH remains close to zero during majority of the year, with the maximum measured so far being 30%.

2.2.2 Auxiliary weather parameters and black carbon

Air temperature and relative humidity are measured by Vaisala HMP45D Pt100 and capacitive sensors. Solar radiation is monitored by Kipp&Zonen CMP3 pyranometer and air pressure by Vaisala PMT16A attached to Vaisala QML201 data logger. Metek USA-1 sonic anemometer is used for wind and turbulence observations. Up to July 2013, we used auxiliary meteorological data measured at the micrometeorological flux cabin located 250 m to the south from station building. Beginning on July 9, 2013 auxiliary data are from the station. In this new location, wind is observed at a 10 m tower instead of the earlier 3 m flux measurement mast. To study the homogeneity of wind observations at station and cabin sites, we excluded calm cases (wind speeds less than 1 m s^{-1}), the same way as was done for the other analysis here. Compared to the wind speed observations at station, wind speed at the cabin was on the average 71 % (correlation coefficient 0.93) and 79 % (correlation coefficient 0.97) lower in summer and winter, respectively. Wind directions were within 30° in 93 % and 87 % of the cases in summer and winter, respectively.

Black carbon at the station is measured with an aethalometer (Magee Scientific, model AE31). The instrument has seven wavelengths of which 880 nm is used to determine the black carbon (BC) mass, assuming a mass absorption cross-section of 16.6 $\mathrm{m^2\ g^{-1}}$. The wavelength of 880 nm was chosen since longer wavelength are less influenced by the presence of brown carbon which is not investigated in detail here (Andreae and Gelencér, 2006; Kirchstetter and Thatcher, 2012). The equivalent BC mass concentrations of the aethalometer is used as such although there exists several different correction schemes for the data (Collaud Coen et al., 2011; Petzold et al., 2013). The most important part of the correction schemes is to compensate for the instrument response as the filter attenuation increases. However, no such general behavior was observed in the data and therefore justifies the data to be used as such.

2.3 Data analysis

All the data are measured and presented in UTC time. The solar midday in Tiksi is around 13:30 local time (22:30 in UTC). No conversion to STP was done, since the site is at a sea level and measurement temperature remains relatively stable around 20 °C.

2.3.1 Data coverage

Due to harsh winter conditions and remoteness of the Tiksi site, in addition to instrument related failures, some of the data were lost in particular during the first two winters (Fig. S2, supplement). The overall data coverage in our DMPS measurements was 74%, but additional 36% of those were lost in data cleaning. The data coverage for APS was 30%, and for meteorological (T, RH, Winds and Radiation) measurements it was 76%.

2.3.2 DMPS data inversion, cleaning and quality checking

DMPS data were inverted using measured flow rates and the default temperature of 293 K and a pressure of 1 atm, using the routine as described in Wiedensohler et al. (2012). Briefly, the data inversion routine uses the charging probabilities defined by Wiedensohler (1989), the transfer functions of Stolzenburg (1988) and takes into account the theoretical diffusion losses of particles in measurement lines and inside the DMAs, as well as accounts for the calibrated CPC detection efficiencies.

As a first step, all data were inverted and manually checked for any instrument or inversion related failures. These data are here referred as all the data available. As a second step, these data were cleaned from any local pollution, which was mainly related with activities in Tiksi city north from the station. Therefore, the wind direction and speed were used as an indication and all data during winds from sector 315–45° were removed, as well as those values measured with wind speeds <1 m s^{-1}. In addition to this, occasional short-term peaks, especially when occurring in Aitken mode sizes, were removed. These peaks might have been caused by variable human activities in the vicinity of the station, for example the personnel transportation to the station using motor vehicles.

For the period of about 10 months (3 July 2013 – 14 May 2014) of coincident DMPS and CPC measurements, the quality of data and that of the DMPS inversion routine were additionally verified by making a comparison of the DMPS total integrated number (in a size range of 7 – 500 nm) and the total number measured by the CPC 3772. A median of CPC number during the size-stepping period of 10 minutes of the overlapping DMPS measurements was used in comparison. A least-square-fit of DMPS versus CPC number as constrained with a zero-intercept forcing, resulted in a slope of 0.98 with a coefficient of determination, R-squared, value of 0.92.

2.3.3 Diameter and density correction to APS

The APS measures the aerodynamic particle sizes while the DMPS measures the particle mobility (equals geometric, assuming a shape factor of one) sizes. The aerodynamic diameters of particles (D_a) are related to mobility diameters

$$D_p = D_a \sqrt{\frac{\rho_0}{\rho_p}} \sqrt{\frac{C_c(D_p)}{C_c(D_a)}}, \tag{1}$$

where ρ_0 is the density of D_a, in this case the unit density of a sphere (1 g cm^{-3}), and ρ_p is the density of D_p. The square-root of the ratio of the slip correction terms (C_c) can be approximated as unity here, since the underestimation due to this is very minor at the size range of question, $D_p > 500$ nm.

To combine our observations we still need to approximate the particle density ρ_p. As a first approximation, we used a value of 1.5 g cm^{-3}, previously reported and largely used for northern Finland boreal forest site (Saarikoski et al., 2005; Viskari et al., 2012). The goodness of this approximation was also tested by matching the APS and DMPS data from the period of overlapping measurements, Jan 16, 2013 – Nov 26, 2013. The APS data was merged with the time frame of the available DMPS measurements using averaging when several APS observations were available from the 10-min period of DMPS measurement cycle. Furthermore, the highest and the lowest 10th percentiles (based on total concentration) were removed from both the DMPS and APS data, leaving 66% of the overlapping data available for the analysis. The density correction to the APS changed the lowest measured diameter size from 500 nm to 410 nm.

The APS showed lower concentrations at the size range where the instruments overlap (Fig. S3, supplement). It is likely that the APS under-counts the particles at its lowest channels, while the DMPS correspondingly suffers from larger statistical errors at its highest channels where the number concentrations are low. Therefore, the three lowest channels of the APS and the highest of the DMPS were discarded from the further analysis, leaving a comparison size range from 493 nm to 658 nm (lower and upper size limit). A scatter of these data yet resulted in a slope of 1.79 (R^2=0.56), the APS underestimating the particle concentration (Fig. S4, supplement). The slope appeared to be slightly steeper in warm months (July–August), possibly indicating a decrease in particle density. However, since both of the instruments used are known to have troubles in their overlapping size range, further corrections (e.g. a correction of a detection efficiency) were not done and thus the coarse mode aerosol concentration derived based on APS data should be interpreted as a lower limit estimate. All the APS data shown here are presented in mobility diameters, assuming the particle density of 1.5 g cm^{-3}.

2.3.4 Calculation of air-mass back-trajectories

Air mass back trajectories at arrival levels of 100, 500 and 1000 m a.s.l. for Tiksi were calculated using a HYSPLIT 4 model (Draxler et al., 1997; Draxler and Hess, 1998; Draxler, 1999). The National Weather Service's National Centers for Environmental Prediction (NCEP) Global Data Assimilation System (GDAS) was used as a meteorological data input for the HYSPLIT model runs. A new trajectory was started every 3h calculating 120h backwards. Trajectories calculated for different arrival heights showed generally very similar paths and for example, the overall calculated average fraction of air masses over the continent was 0.70, 0.68 and 0.69 for 100, 500 and 1000 m heights, respectively.

2.3.5 Clustering of size distributions

Cluster analysis technique was applied to divide particle size distributions into five (5) mutually different, but internally similar groups. K-means clustering algorithm, previously denoted as an efficient and well qualified method for clustering particle size distributions (Beddows et al., 2009), was used for minimizing the within cluster variance (sum of squared Euclidean distances from cluster centers). Number of clusters was chosen based on several test runs with different number of clusters. The initial cluster centroid positions for the iterative algorithm were chosen randomly, which however, based on several consecutive runs did not affect the final cluster composition significantly.

2.3.6 Analysis of new particle formation and growth

The four years of DMPS measurements were analysed for new particle formation events and their characteristics. Days with new particle formation (NPF) were identified from the data using the methodology as developed by Dal Maso et al. (2005). According to the methodology, any days showing particles below 25 nm size range with growth of this nucleation mode are classified as event days. The days with uninterrupted growth starting at the smallest measurable size of 7 nm where is possible to calculate the NPF related statistics are further classified as event class I. In contrast, class II events present more concentration fluctuations and thereby, the particle growth rates or formation rates are not possible to calculate. Days of no growth or growth of the larger Aitken mode particles are classified as undefined days. Days with no particles at nucleation mode sizes are those of non-event days. Additionally, days with missing or bad data are defined as unclassified.

For class I events, also the particle growth rates and formation rates were calculated using the exact same method as in Asmi et al. (2011), for analyzing the NPF in northern Finland. Particle growth rates (nm h^{-1}) were calculated following the growing mode peak diameter and the particle formation rates (at 7 nm size) by following the increase of nucleation mode number concentration with time with a user input of mode maximum diameter. In comparison to the analysis presented by Kulmala et al. (2001), also extra-modal coagulation losses were taken into account, i.e. the losses of nucleation mode particles to bigger particle sizes. The particle atmospheric diameters were calculated using hygroscopicity parameterisation for boreal forest conditions as presented by Laakso et al. (2004).

3 Results

3.1 Seasonal cycles of meteorological variables

Meteorological conditions (Fig. 2) in Tiksi display large annual variability that is controlled by alternating periods of the polar night (Nov 19 – Jan 24) and the midnight sun (Jun 11 – Aug 03). With respect to the variables analyzed (i.e. temperature, RH, radiation, winds and air mass origin), the years from 2010 to 2014 had similar seasonal cycles. Median temperatures stayed above zero for four months each year between June and September. This period was also characterized by the highest frequency occurrence of marine air masses, the highest absolute values and variability in relative humidity, and the most stable wind speeds with median values extending from 3 to 5 m s^{-1}. A shift occurred in October with decreased solar insolation resulting in a temperature shift to below zero. RH decreases were correlated with the decreasing temperature until January–February, after which the increasing solar radiation resulted in an increasing temperature and RH. The cold month winds were primarily as continental with low frequency occurrence of marine air masses. In October through December, very high wind speeds occurred with half hour averages of up to 20 m s^{-1} indicating stormy weather conditions. January through March was the calmest period of the year with median wind speeds between 1 and 3 m s^{-1}. A shift in weather conditions occurred in April–May with increasing temperatures and stronger winds and the onset of more frequent marine air flow. Precipitation data was examined from the Russian Roshydromet weather observations for years 2010–2014. During the analysis period, most precipitation occurred in July–August when the monthly average precipitation amounts were $>$50 mm. The driest seasons where February–May and October–November when the monthly average precipitation was $<$20 mm.

3.2 Temporal variability of aerosol numbers and mass

The total particle number concentrations (Fig. 3 and Table 1) showed two annual maxima in March and in July. For further details on this annual cycle, the particle size distributions were further divided into four characteristic modes: nucleation (7–25 nm), Aitken (25–100 nm), accumulation (100–500 nm) and coarse ($>$410 nm from APS, when available), and the annual cycle of each of these modes was analysed separately. It can be seen that for the nucleation and Aitken mode particles the July maxima in number are the highest whereas for the accumulation and coarse mode particles the March maxima are higher. The particle mass concentration maxima in March became even more dominant and persisted through the months of late winter and spring (Fig. 4 and Table 1). This indicates the significant influence of Arctic haze, which primarily increases the larger particle number and mass concentration suggesting impacts via indirect aerosol effects and atmospheric visibility. Similar behavior could also be seen in seasonal cycles of size distributions where the

Aitken mode was the most dominant only during June–August and a strong accumulation mode was observed in spring months (Fig. S5, supplement).

Compared to the aerosol number size distributions measured in northern Finland at the Pallas and Värriö Arctic sites (Laakso et al., 2003; Tunved et al., 2003), the distributions in Tiksi show similar seasonal variability but with lower concentrations throughout the year. Instead, compared to measurements in higher latitude Arctic sites at Barrow and Zeppelin the number concentration in Tiksi is higher especially during spring and summer (Bodhaine, 1989; Tunved et al., 2013). The mass concentrations in Tiksi presents a similar annual variability as those measured at Barrow and Zeppelin sites but a quantitative comparison between them was difficult due to different methods and size ranges used (Quinn et al., 2002; Tunved et al., 2013).

Nucleation mode particles are indicative of the secondary production processes taking place in the Arctic. A clear minimum in nucleation mode concentration was observed in January. Concentration increased again with the increasing seasonal solar radiation indicating a photochemically driven process. Despite the high particle mass during the Arctic haze period, secondary production of particles also appeared to take place as soon as solar radiation was available. This is opposite to what is seen at the high-latitude Arctic sites Barrow and Zeppelin (Bodhaine, 1989; Tunved et al., 2013) but similar to what is observed at a continental northern Finland Arctic site Pallas (Asmi et al., 2011). The origin of the nucleating and condensing vapors may therefore be connected with regional continental sources, in addition to what is contained in the haze itself. However, the long-range transported haze aerosols are also likely to be important for the secondary particle formation and growth process since after the dissipation of Arctic haze later in the spring, the nucleation mode concentrations decrease. A second nucleation mode maximum follows in summer, likely attributable to vegetation related biogenic sources.

3.3 Aerosol size distributions clusters

In addition to the seasonal cycles of aerosol size distribution modes, a number of factors could potentially produce specific type of number or mass size distributions. To elucidate any specific size distribution types, and to study the impact of different environmental conditions on the modal characteristics of aerosol size distributions, we used cluster analysis as described in section 2.3.5. For this, the quality controlled DMPS data (diameter range from 7 to 500 nm) were clustered into five mutually dissimilar groups using the methodology explained in section 2.3.5. A median of 1.5 hour distributions were used in order to catch the typical features corresponding to the different air mass types (3h time resolution) as well as to the variable meteorological parameters (0.5h time resolution).

As a result of this clustering, most of the data appears to fall into a category of bi-modal number size distributions, with maxima in Aitken and accumulation modes at sizes 50–70 and 200 nm, respectively (Fig. 5a). Cluster 1 had the highest number concentration with elevated concentrations especially in Aitken mode. An increase of an Aitken mode aerosols indicates the proximity of local sources in addition to long-range transport represented by the accumulation mode. Looking at the meteorological parameters in Table 2 it can be seen that this type of size distributions occurred during cold winter days and they coincided with elevated black carbon (BC) concentrations, thereby indicating strong inversions trapping local pollutants originating in combustion sources. Winds were calm and air masses mainly continental, as during most of the winter. However, size distributions representative of cluster 1 are rare, and only 70 cases were identified in our analysis. Cluster number 2, which also presents elevated number concentrations, but clearly less severe pollution episodes, instead were more common and present also on other seasons. In summer, aged biomass burning aerosols could be included in this cluster type. This was also the cluster of most continental influences. The remaining clusters numbers 3–5 present more clean air masses with no local influences, as seen from their lower BC concentrations. Cluster number 3 was the most common cluster type observed, and it had both continental and marine influences, and the lowest average number concentration ($301 \pm 243\,\mathrm{cm}^{-3}$) of all the clusters. Cluster 4 was very specific to strong cases of secondary particle formation as seen by its high number concentration especially in nucleation mode. Interestingly, this cluster type contained mostly marine influences, and was connected with high solar radiation, as indicative of photochemical processes. It appears that nucleation is more common in marine as opposed to continental, air masses; this phenomena has been documented in previous studies (Sogacheva et al., 2008; Asmi et al., 2011). Compared to the other clean cluster types 5 and 3, cluster 4 had also the lowest values of RH. Increasing RH and decreasing radiation could be linked with cloudiness inhibiting nucleation (Sogacheva et al., 2008; Hamed et al., 2011). Interestingly, nucleation seemed also less likely with increasing wind speeds which might be explained by more efficient dilution of the nucleating and condensing vapors or by the scavenging of nucleating clusters. This further implies that nucleation at Tiksi is connected to sources near the surface, most likely to biogenic VOC emissions. As secondary aerosols are aged, the particle number concentrations decrease and move towards larger sizes, which appears to be represented in the remaining cluster number 5. Secondary particle formation as a source of aerosols in Tiksi will be further analysed in the following section.

Similar clustering analysis was done for the mass size distributions, with assumed particle density of 1.5 g cm^{-3} (Figs. 5b and Table 3). APS data were not used in clustering due to poor data coverage, however, the results for coarse mode (when available) are presented.

Two first mass clusters, numbers 1 and 2, present cases of extremely high mass concentrations with averages of 52.1 and 18.4 μg m^{-3} (from DMPS only) respectively, and also elevated BC with concentrations up to 2 μg m^{-3}. These clusters are characterized by strong continental influences, and high average temperatures, indicating that they occur in summer continental air flows. Cluster 1 occurred only on July 9 and 11, 2012 and represent a strong case of long-range transport of biomass burning (BB) aerosols from the southern Yakutian region, as indicated by MODIS active fire records combined with back-trajectory calculations. Further, the days inside of cluster 2 are: July 26, 2012, August 1–2, 2012, September 25–26, 2012, and August 12–13, 2013. For all these days the back-trajectory calculations also indicated transport from southerly directions, where MODIS recorded forest fire activity; simultaneously, the measured BC concentration at Tiksi was elevated to around 1 μg m^{-3}. Cluster 3 has also elevated mass concentrations and similar average BC to mass ratios than clusters 1 and 2. Cluster 3 occurred both in early spring and in summer and showed an average mass concentration of 5.8 μg m^{-3}. This is less than the concentrations characterizing the biomass burning episodes, yet clearly higher than concentrations typical to Tiksi. Average temperature for cluster 3 was high (6.5 °C), values of global radiation were the highest and RH was the lowest of all the clusters. It seems therefore likely that this cluster represents summer continental air masses that were strongly affected by the biogenic sources and the secondary particle formation. Since the process of secondary particle formation from biogenic precursors is dependent on light providing the atmospheric oxidizing capacity, the conditions of high radiation and low RH (indicating low cloudiness) are favorable for this process (Hamed et al., 2011). If continental clusters typically have high mass concentrations, cluster 4 has the lowest mass concentration and is representative of very clean marine air. It occurred year-round but was the most prevalent during summer and autumn. The last cluster number 5 was mixed between continental and marine influence. Mass concentration was clearly increased as compared with cluster 4 but the most interestingly, ratio of black carbon was about twice as high as in any other cluster. Cluster 5 was mainly observed in early spring and is therefore likely to best represent the cases of Arctic haze and long-range transported aerosol influences.

3.4 Secondary particle formation in Tiksi

Secondary particle formation was also identified as an important source of aerosol in Tiksi, with one example of an event observed plotted in Figure S6, supplement. In section 3.2 we have seen that nucleation mode concentrations were elevated particularly during spring and summer, which already gives indications of the seasonal variability of particle formation. This process was further studied using the methodology described in section 2.3.6.

Firstly, based on Dal Maso et al. (2005), we classified the measurement days into event, non-event and undefined cases, to study the frequency of the particle formation in different seasons. Monthly fraction of each of these classes is presented in Figure 6, and shows that secondary particle formation in Tiksi is most frequent in early spring (March) and in summer (June–August). In March a particle formation event was observed on nearly half of the days and in summer on 30–40 % of the days. Events get less frequent towards autumn, similar to what is seen on other Arctic site Pallas, in northern Finland (Asmi et al., 2011). Also seasonal cycle of event frequency resembles that observed in Pallas, however, particle formation is seen almost twice as frequent in Tiksi in comparison to Pallas site (Asmi et al., 2011). Compared to another typical boreal forest site in southern Finland, the event frequencies in Tiksi are comparable but differ slightly in seasonal cycle (Dal Maso et al., 2005). Similar detailed analysis of the secondary particle formation has not been done for any other Arctic sites. However, based on aerosol modal variability, events at the Arctic Zeppelin station appear to follow seasonal pattern similar to Tiksi and Pallas (Tunved et al., 2013).

Even if events in Tiksi were frequent, class 1 events starting at 7 nm size and showing a well defined growing mode, were rare. For this reason the particle formation and growth rate parameters were also calculated for as many class 2 events as was feasible (remaining were classified as class 3, see Fig. 6). The inter-annual cycle of particle formation and growth rates were clear (Fig. 7 and Table 4). Growth rate maximum (3.6 nm h^{-1}) was in July and minimum (0.1 nm h^{-1}) in December. Average growth rates of over 2 nm h^{-1} were only seen in summer months: June to August, suggesting an important role of biogenic emissions as well as photochemistry of the compounds responsible for the growth. This is similar to what has been observed on other boreal forest sites (e.g., Tunved et al., 2003; Dal Maso et al., 2005; Asmi et al., 2011). However, compared to other measurement sites closer to forested areas, particle growth rates in Tiksi were lower, and especially in autumn and winter, many examples of extremely low growth rate were observed. Nucleation mode particles with very limited growth have also been observed during polar night in Antarctica (Järvinen et al., 2013; Weller et al., 2015).

The particle formation rates, instead, were peaking in early spring, with maximum value of 0.25 cm^{-3} s^{-1} observed in March. During winter, in the lack of photochemistry, the particle formation rates were extremely small, being only around 0.01 cm^{-3} s^{-1}. This annual cycle is in line with previous observations (e.g., Dal Maso et al., 2005; Asmi et al., 2011) and suggests that the same precursor compounds that lead to the formation of Arctic haze (i.e. SO2) also contribute to the regional-scale NPF events during spring.

Comparing the class 1 and class 2 formation and growth parameters, the class 1 events are stronger and also present higher particle growth rates (Table 4). For class 2 events the presented formation rates are the lower estimates while a new mode did not always appear at the lowest measurable 7 nm size. The seasonal cycle however is similar to both event classes.

Finally, the origin of air masses on event days and non-event days was studied (Fig. 8). Indeed, it appears that on non-event days continental air flows were typical, while on event days such a tendency was not detected. On event days, coastal and marine air masses seemed to be slightly more common, as compared with non-event or undefined days. But the origin alone seem not to divide the days that clearly it would provide a plausible explanation for particle formation. Neither it gives a clear indication of the origin of the secondary particles, weather they are continental, coastal or marine.

3.5 Continental biogenic sources driving the cloud condensation nuclei concentrations in summer

Similar to previous observations in the boreal forest zone (Tunved et al., 2006; Asmi et al., 2011; Väänänen et al., 2013), observations at Tiksi indicate increasing submicron aerosol particle mass with increasing time over continent (Fig. 9). The increase was larger by an order of magnitude when temperature exceeded 0 °C, although at temperatures <0 °C some increase in aerosol mass could be still observed with longer time over continent (Fig. 9b). This is expected considering the strong temperature dependency of biogenic VOC emissions (e.g., Guenther et al., 2006).

Another temperature dependent feature affecting aerosols in Tiksi are the frequent Siberian fires (BB events). Results of the clustering analysis were used to assist in separating the four BB event cases observed in summer 2012 and the one BB event case in summer 2013, to isolate their impact in overall result. The aerosol mass and number concentration addition with and without inclusion of these events was analyzed separately.

Tunved et al. (2006) showed that the aerosol mass load over the Finnish Arctic site Pallas depends on the air mass time over the continent and follows a linear fit $y = 0.014x + 0.12$, where y represents the aerosol mass [μg m^{-3}] and x the time [h] spent over the continent and April–September DMPS data for sizes $<$ 450 nm were used for fitting. Fitting for the

Tiksi data was also done using only summertime data and particle sizes $<$ 500 nm; the resulting fit y = 0.018x – 0.05 (Fig. 10a), indicates a similar or even higher, mass increase over the Siberian continental region in comparison to Nordic boreal forest. Exclusion of BB events decreased the slope from 0.018 to 0.016 μg m^{-3} h^{-1}, yet it must be kept in mind that only the impact of the strongest five events was studied here. Additionally, Tiksi data suggests rather exponential than linear dependence between aerosol mass and time over continent; Exponential fit results in improvement of R_2 value from 0.84 to 0.93 (and from 0.88 to 0.94 for no-BB cases). This might be a secondary effect of the observed temperature dependence of the continental air masses. The most continental air masses also possessed the warmest temperatures, therefore it is likely that they originate further from the south, with denser vegetation as well as higher VOC emission rates (Guenther et al., 2006).

As a direct consequence of secondary aerosol formation, the number of the largest particles that are capable of acting as cloud condensation nuclei (CCN), tends to increase. This has been shown for several sites that were characterized by relatively clean and cold environments and affected by biogenic VOCs by Paasonen et al. (2013). They also linked the CCN concentrations with measured monoterpenes. In their study Paasonen et al. (2013) used aerosol number concentration over the limit of 100 nm as a proxy for the CCN, which will be here referred to as CCN_{100}.

In Tiksi, the CCN_{100} concentration also increased as a function of temperature (Fig. 10b). While the average CCN_{100} concentration remained below 200 cm^{-3} throughout most of the year, at $>$10 °C an exponential increase as a function of temperature was observed. Paasonen et al. (2013) also showed an increase of CCN_{100} as a function of temperature with exponential fits for two Finnish, one Canadian and one Russian Siberian sites. When CCN_{100} [cm^{-3}] was fitted as a function of temperature (T)

$$CCN_{100} = \alpha \exp(\beta T) \tag{2}$$

they obtained β values varying between 0.029 and 0.085 ^{o}C^{-1}. Here the α is a fitting variable having a unit [cm^{-3}]. Data from Tiksi plotted for a similar temperature range $>$ 5°C, show even a higher temperature dependence with β value of 0.126 ^{o}C^{-1} (Fig.10b). Again, exclusion of the BB events did not change the β value significantly, yet the data follow better the exponential fitting line when the strong BB events are not included. This confirms a major biological contribution to Tiksi aerosol populations during summer and suggests a strong temperature feedback for the aerosols in Arctic Siberia. Possible reasons for the deviating temperature dependencies observed for the five different sites include differences in the relative importance of other (anthropogenic) sources as well as the different vegetation types. In comparison to European boreal forest emissions, which are largely dominated by α-pinene (Rinne et al., 2000; Tarvainen et al., 2005), Siberian larches emit mainly sabinene (Ruuskanen et al., 2007) leading to different oxidation chemistry and consequently different aerosol yields (e.g., Griffin et al., 1999). In addition to the natural vegetation sources, another temperature dependent aerosol source in summer Siberia are the intense fire events which based on (Fig.10b) appear to increase the CCN_{100} numbers occasionally.

In context of the entire Tiksi annual temperature range, the maximum average CCN_{100} concentration of 1130 cm^{-3} was observed at temperatures >30 °C (Fig.11a). However, these extreme hot days are rare in Tiksi and only 13 cases were available for calculations. The average CCN_{100} concentrations were lower in marine in comparison to continental air masses. The increase of CCN_{100} with temperature was only observed in continental air masses, providing further evidence of the importance of continental biogenic VOC or fire related sources. However, the comparison of continental and marine air masses is somewhat obscured by the lack of warm Arctic marine air.

The CCN_{100} concentrations can be compared with the total aerosol number concentrations to indicate changes in the aerosol number size distributions. Ratio of these numbers stayed around 0.5 during most of the year in both of the air mass types (Figure 11b). However, during summer (at temperatures above zero), this ratio decreased to close to 0.1 in marine air masses, thus indicating an increasing total number concentration caused by the smallest particles. In continental air masses the CCN_{100} to number ratio showed an incremental decrease as a function of temperature in the range of 0–15 ^{o}C, which was followed by a strong increase of CCN_{100} with temperature. In a global perspective this result can be compared with those of Andreae (2009) indicating that the CCN and particle number concentrations and their ratios in Tiksi are well representative for either remote marine or continental site, depending on the air mass origin.

3.6 Accumulation of pollutants on calm and cold winter days

There are many indications in the Tiksi data of a severe pollution occurring during cold and calm weather. This was studied in detail when wind speeds decreased to values close to 1 m s^{-1} (a threshold for data quality checks) resulting in increasing number concentrations (Fig. S7, supplement). This was particularly true for the Aitken mode particles, indicating an influence from local or regional pollution sources, but CCN$_{100}$ concentrations in the accumulation mode were also elevated during the coldest episodes. As these are likely caused by strong cold-weather inversions, and contain episodes lasting for hours or even days, it is not clear if these should be considered as local air pollution events and removed from the analysis, or rather as more regional pollution occurring over vast areas in northern Siberia. At wind speeds $>$ 2 m s^{-1} such pollution episodes became rare and therefore, in order to exclude them this limit could be used. However, calm days were common during winter months and their exclusion also removes a large fraction of wintertime data.

4 Conclusions

Aerosols measured in Tiksi show a large seasonal variability in terms of particle size, number and mass distributions. The monthly median total aerosol number concentration in Tiksi ranges from 184 cm^{-3} in November to 724 cm^{-3} in July with a local maximum in March of 481 cm^{-3}. Nucleation mode particles are frequently observed in Tiksi during early spring and summer and the formation of these particles is favored in marine air masses. This suggests either a marine source of nucleating vapors or a lower background concentration and thereby a decreased sink for particles and vapors at a coastal zone.

Detailed analysis of secondary particle formation events in Tiksi during 2010–2014 showed that this process takes place on nearly 50 % of the days in March and on 30–40 % of the days during summer (June–August). Some sporadic events are also observed during dark winter months, providing evidence that the formation of secondary particles can take place even in the lack of photo-chemistry. Particle formation rates are the highest in spring (March–May) while the growth rates are the highest in summer (June-August). This suggests that there are effectively two types of particle formation events: 1) the high formation rate events in early spring, originating in the oxidation of anthropogenic emissions accumulated over winter, where the source is essentially the same as for the Arctic haze, and 2) the summertime high growth rate events, which are likely driven by BVOC oxidation in the presence of low-sink.

The influence of the vast, vegetated Siberian regions on aerosol characteristics is the most evident in summer when the number concentration reaches a maximum. This is related to secondary particle formation and growth by biogenic organic compounds, and to some extent also on biomass burning. By using a cluster analysis, five strong fire events were isolated showing that biomass burning can have an impact all the way north in the Arctic. The biogenic and biomass burning related sources increase the particle number, but also the mass and the concentrations of cloud condensation nuclei (CCN), thereby being important modulators of the summertime Arctic climate. Increase of the CCN and particle mass are only seen in continental air masses, and have a strong correlation with the temperature.

The total mass concentration has a distinct maximum in February–March of 1.72–2.38 μg m^{-3} and two minimums in June of 0.42 μg m^{-3} and in September–October of 0.36–0.57 μg m^{-3}. In winter and spring, the size distributions are dominated by larger accumulation and coarse mode particles influenced by Arctic haze. Elevated mass concentrations are measured until April after which another maximum in mass occurs in July–August. The second mass maximum is lower in amplitude and mainly results from increased accumulation mode aerosol mass distributions rather than coarse mode aerosol mass distributions. Additionally, during calm and cold winter periods, severe pollution episodes can occur due to the local inversions leading to an accumulation of particles close to the surface.

The results presented here highlight some of the important mechanisms that control the Russian Arctic aerosol size distributions and sets the stage for quantitative future studies on their source identification.

Acknowledgements. This work was supported by the Academy of Finland project Greenhouse gas, aerosol and albedo variations in the changing Arctic (project number 269095) and the Academy of Finland Center of Excellence program (project number 272041), KONE foundation (grant number 46-6817) and Magnus Ehrnooth foundation grant for “Natural climate feedbacks of aerosols in the Arctic”. Data collection, acquisition, transfer and archiving was supported by the Roshydromet Arctic and Antarctic Research institute and the NOAA Earth Systems Research Laboratory Physical Science Division. We also like to thank E.D. Volkov and O.V. Dmitrieva for maintaining the measurements in Tiksi year-round.

References

Andreae, M. O. and Gelencsér, A.: Black carbon or brown carbon? The nature of light-absorbing carbonaceous aerosols, Atmos. Chem. Phys., 6, 3131–3148, doi:10.5194/acp-6-3131-2006, 2006.

Andreae, M. O.: Correlation between cloud condensation nuclei concentration and aerosol optical thickness in remote and polluted regions, Atmos. Chem. Phys., 9, 543–556, doi:10.5194/acp-9-543-2009, 2009.

Asmi, E., Kivekäs, N., Kerminen, V.-M., Komppula, M., Hyvärinen, A.-P., Hatakka, J., Viisanen, Y., and Lihavainen, H.: Secondary new particle formation in Northern Finland Pallas site between the years 2000 and 2010, Atmos. Chem. Phys., 11, 12959-12972, doi:10.5194/acp-11-12959-2011, 2011.

Asmi, E., Freney, E., Hervo, M., Picard, D., Rose, C., Colomb, A., and Sellegri, K.: Aerosol cloud activation in summer and winter at puy-de-Dôme high altitude site in France, Atmos. Chem. Phys., 12, 11589–11607, doi:10.5194/acp-12-11589-2012, 2012.

Beddows, D. C. S., Dall’Osto, M., and Harrison, R. M.: Cluster Analysis of Rural, Urban, and Curbside Atmospheric Particle Size Data, Environ. Sci. Technol., 43, 4694–4700, doi: 10.1021/es803121t, 2009.

Bodhaine, B. A.: Barrow surface aerosol – 1976–1986, Atmos. Environ., 23, 2357–2369, doi:10.1016/0004-6981(89)90249-7, 1989.

Bond, T. C., Doherty, S. J., Fahey, D. W., Forster, P. M., Berntsen, T., DeAngelo, B. J., Flanner, M. G., Ghan, S., Kärcher, B., Koch, D., Kinne, S., Kondo, Y., Quinn, P. K., Sarofim, M. C., Schultz, M. G., Schulz, M., Venkataraman, C., Zhang, H., Zhang, S., Bellouin, N., Guttikunda, S. K., Hopke, P. K., Jacobson, M. Z., Kaiser, J. W., Klimont, Z., Lohmann, U., Schwarz, J. P., Shindell, D., Storelvmo, T., Warren, S. G., and Zenderm C. S.: Bounding the role of black carbon in the climate system: a scientific assessment, J. Geophys. Res.-Atmos., 118, 5380–5552, doi:10.1002/jgrd.50171, 2013.

Bourgeois, Q., and Bey, I.: Pollution transport efficiency toward the Arctic: Sensitivity to aerosol scavenging and source regions, J. Geophys. Res., 116, D08213, doi: 10.1029/2010JD015096, 2011.

Chi, X., Winderlich, J., Mayer, J.-C., Panov, A. V., Heimann, M., Birmili, W., Heintzenberg, J., Cheng, Y., and Andreae, M. O.: Long-term measurements of aerosol and carbon monoxide at the ZOTTO tall tower to characterize polluted and pristine air in the Siberian taiga, Atmos. Chem. Phys., 13, 12271–12298, doi:10.5194/acp-13-12271-2013, 2013.

Collaud Coen, M., Weingartner, E., Apituley, A., Ceburnis, D., Fierz-Schmidhauser, R., Flentje, H., Henzing, J. S., Jennings, S. G., Moerman, M., Petzold, a., Schmid, O. and Baltensperger, U.: Minimizing light absorption measurement artifacts of the Aethalometer: evaluation of five correction algorithms, Atmos. Meas. Tech., 3(2), 457–474, doi:10.5194/amt-3-457-2010, 2010.

Dal Maso, M., Kulmala, M., Riipinen, I., Wagner, R., Hussein, T., Aalto, P. P., and Lehtinen, K. E. J.: Formation and growth of fresh atmospheric aerosols: eight years of aerosol size distribution data from SMEAR II, Hyytiälä, Finland, Boreal Environ. Res., 10, 323–336, 2005.

Draxler, R.R., and G.D. Hess: Description of the HYSPLIT_4 modeling system. NOAA Tech. Memo. ERL ARL-224, NOAA Air Resources Laboratory, Silver Spring, MD, 24 pp, 1997.

Draxler, R.R., and G.D. Hess: An overview of the HYSPLIT_4 modeling system of trajectories, dispersion, and deposition. Aust. Meteor. Mag., 47, 295–308, 1998.

Draxler, R.R.: HYSPLIT4 user's guide. NOAA Tech. Memo. ERL ARL-230, NOAA Air Resources Laboratory, Silver Spring, MD, 1999.

Eckhardt, S., Quennehen, B., Olivié, D. J. L., Berntsen, T. K., Cherian, R., Christensen, J. H., Collins, W., Crepinsek, S., Daskalakis, N., Flanner, M., Herber, A., Heyes, C., Hodnebrog, Ø., Huang, L., Kanakidou, M., Klimont, Z., Langner, J., Law, K. S., Lund, M. T., Mahmood, R., Massling, A., Myriokefalitakis, S., Nielsen, I. E., Nøjgaard, J. K., Quaas, J., Quinn, P. K., Raut, J.-C., Rumbold, S. T., Schulz, M., Sharma, S., Skeie, R. B., Skov, H., Uttal, T., von Salzen, K., and Stohl, A.: Current model capabilities for simulating black carbon and sulfate concentrations in the Arctic atmosphere: a multi-model evaluation using a comprehensive measurement data set, Atmos. Chem. Phys., 15, 9413–9433, doi:10.5194/acp-15-9413-2015, 2015.

Griffin, R. T., Cocker III, D. R., Flagan, R. C. and Seinfeld, J. H.: Organic aerosol formation from the oxidation of biogenic hydrocarbons, J. Geophys. Res., 104(D3), 3555–3567, 1999.

Guenther, A., Karl, T., Harley, P., Wiedinmyer, C., Palmer, P. I., and Geron, C.: Estimates of global terrestrial isoprene emissions using MEGAN (Model of Emissions of Gases and Aerosols from Nature), Atmos. Chem. Phys., 6, 3181–3210, doi:10.5194/acp-6-3181-2006, 2006.

Hamed, A., Korhonen, H., Sihto, S.-L., Joutsensaari, J., Järvinen, H., Petäjä, T., Arnold, F., Nieminen, T., Kulmala, M., Smith, J. N., Lehtinen, K. E. J., and Laaksonen, A.: The role of relative humidity in continental new particle formation, J. Geophys. Res., 116, D03202, doi:10.1029/2010JD014186, 2011.

Heintzenberg, J., Birmili, W., Theiss, D., and Kisilyakhov, Y.: The atmospheric aerosol over Siberia, as seen from the 300m ZOTTO tower, Tellus, 60B, 276–285, 2008.

Heintzenberg, J., Birmili, W., Otto, R., Andreae, M. O., Mayer, J.-C., Chi, X., and Panov, A.: Aerosol particle number size distributions and particulate light absorption at the ZOTTO tall tower (Siberia), 2006–2009, Atmos. Chem. Phys., 11, 8703–8719, doi:10.5194/acp-11-8703-2011, 2011.

Hienola, A. I., Pietikäinen, J.-P., Jacob, D., Pozdun, R., Petäjä, T., Hyvärinen, A.-P., Sogacheva, L., Kerminen, V.-M., Kulmala, M., and Laaksonen, A.: Black carbon concentration and deposition estimations in Finland by the regional aerosol–climate model REMO-HAM, Atmos. Chem. Phys., 13, 4033–4055, doi:10.5194/acp-13-4033-2013, 2013.

Hinds, W. C.: Aerosol Technology: Properties, Behaviour and Measurement of Airborne Particles, 2nd Edn., John Wiley, New York, 1999.

Järvinen, E., Virkkula, A., Nieminen, T., Aalto, P. P., Asmi, E., Lanconelli, C., Busetto, M., Lupi, A., Schioppo, R., Vitale, V., Mazzola, M., Petäjä, T., Kerminen, V.-M., and Kulmala, M.: Seasonal cycle and modal structure of particle number size distribution at Dome C, Antarctica, Atmos. Chem. Phys., 13, 7473–7487, doi:10.5194/acp-13-7473-2013, 2013.

Kirchstetter, T. W. and Thatcher, T. L.: Contribution of organic carbon to wood smoke particulate matter absorption of solar radiation, Atmos. Chem. Phys., 12(14), 6067–6072, doi:10.5194/acp-12-6067-2012, 2012.

Kulmala, M., Dal Maso, M., Mäkelä , J. M., Pirjola, L., Väkevä, M., Aalto, P., Miikkulainen, P., Hämeri, K., and O'Dowd, C.: On the formation, growth, and composition of nucleation mode particles, Tellus, 53B, 47990, 2001.

Laakso, L., Hussein, T., Aarnio, P., Komppula, M., Hiltunen, V., Viisanen, Y. and Kulmala, M.: Diurnal and annual characteristics of particle mass and number concentrations in urban, rural and Arctic environments in Finland, Atmos. Environ., 37(9), 2629–2641, 2003.

Laakso, L., Petäjä, T., Lehtinen, K. E. J., Kulmala, M., Paatero, J., Hõrrak, U., Tammet, H., and Joutsensaari, J.: Ion production rate in a boreal forest based on ion, particle and radiation measurements, Atmos. Chem. Phys., 4, 1933–1943, doi:10.5194/acp-4-1933-2004, 2004.

Liu, X., Easter, R. C., Ghan, S. J., Zaveri, R., Rasch, P., Shi, X., Lamarque, J.-F., Gettelman, A., Morrison, H., Vitt, F., Conley, A., Park, S., Neale, R., Hannay, C., Ekman, A. M. L., Hess, P., Mahowald, N., Collins, W., Iacono, M. J., Bretherton, C. S., Flanner, M. G., and Mitchell, D.: Toward a minimal representation of aerosols in climate models: description and evaluation in the Community Atmosphere Model CAM5, Geosci. Model Dev., 5, 709–739, doi:10.5194/gmd-5-709-2012, 2012.

Mauritsen, T., Sedlar, J., Tjernström, M., Leck, C., Martin, M., Shupe, M., Sjogren, S., Sierau, B., Persson, P. O. G., Brooks, I. M., and Swietlicki, E.: An Arctic CCN-limited cloud-aerosol regime, Atmos. Chem. Phys., 11, 165–173, 2011.

Mitchell, J. M.: Visual range in the polar regions with particular reference to the Alaskan Arctic, J. Atmos. Terr. Phys., 17, 195–211, 1957.

Paasonen, P., Asmi, A., Petäjä, T., Kajos, M. K., Äijälä, M., Junninen, H., Holst, T., Abbatt, J.P.D., Arneth, A., Birmili, W., van der Gon, H.D., Hamed, A., Hoffer, A., Laakso, L., Laaksonen, A., Leaitch, W.R., Plass-Dülmer, C. Pryor, S.C., Räisänen, P., Swietlicki, E., Wiedensohler, A., Worsnop, D.R., Kerminen, V.-M. and Kulmala, M.: Warming-induced increase in aerosol number concentration likely to moderate climate change, Nat. Geosci., 6, 438–442, doi:10.1038/ngeo1800, 2013.

Petzold, a., Ogren, J. a., Fiebig, M., Laj, P., Li, S. M., Baltensperger, U., Holzer-Popp, T., Kinne, S., Pappalardo, G., Sugimoto, N., Wehrli, C., Wiedensohler, a. and Zhang, X. Y.: Recommendations for reporting black carbon measurements, Atmos. Chem. Phys., 13, 8365–8379, doi:10.5194/acp-13-8365-2013, 2013.

Quinn, P. K., Miller, T. L., Bates, T. S., Ogren, J. A., Andrews, E., and Shaw, G. E.: A 3-year record of simultaneously measured aerosol chemical and optical properties at Barrow, Alaska, J. Geophys. Res.-Atmos., 107(D11), 4130, doi:10.1029/2001JD001248, 2002.

Richter-Menge, J., Overland, J., Proshutinsky, A., Romanovsky, V., Bengtsson, L., Brigham, L., Dyurgerov, M., Gascard, J.C., Gerland, S., Graversen, R., Haas, C., Karcher, M., Kuhry, P., Maslanik, J., Melling, H., Maslowski, W., Morison, J., Perovich, D., Przybylak, R., Rachold, V., Rigor, I., Shiklomanov, A., Stroeve, J., Walker, D. and Walsh J.: State of the Arctic Report. NOAA OAR Special Report, NOAA/OAR/PMEL, Seattle, WA, 36 pp, 2006.

Rinne, J., Hakola, H., Laurila, T. and Rannik, U: Canopy scale monoterpene emissions of pinus sylvestris dominated forests, Atm. Env., 34, 1099–1107, doi: 10.1016/S1352-2310(99)00335-0, 2000.

Ruuskanen, T. M., Kajos, M., Hellén, H., Hakola, H., Tarvainen, V., and Rinne, J.: Volatile organic compound emissions from Siberian larch, Atmos. Environ., 41, 5807–5812, 2007.

Saarikoski, S., Mäkelä, T., Hillamo, R., Aalto, P. P., Kerminen, V.-M., and Kulmala, M.: Physico-chemical characterization and mass closure of size-segregated atmospheric aerosols in Hyytiälä, Finland, Boreal Env. Res., 10, 385–400, 2005.

Shindell, D., and Faluvegi, G.: Climate response to regional radiative forcing during the twentieth century, Nature Geosci., 2, 294–300, 2009.

Sogacheva, L., Saukkonen, L., Nilsson, E. D., Dal Maso, M., Schultz, D. M., De Leeuw, G., and Kulmala, M.: New aerosol particle formation in different synoptic situations at Hyytiälä Southern Finland, Tellus, 60B, 485–494, 2008.

Stock, M., Ritter, C., Aaltonen, V., Aas, W., Handorff, D., Herber, A., Treffeisen, R., and Dethloff, K.: Where does the optically detectable aerosol in the European Arctic come from?, Tellus B, 66, 21450, http://dx.doi.org/10.3402/tellusb.v66.21450, 2014.

Stohl, A., Klimont, Z., Eckhardt, S., Kupiainen, K., Shevchenko, V. P., Kopeikin, V. M., and Novigatsky, A. N.: Black carbon in the Arctic: the underestimated role of gas flaring and residential combustion emissions, Atmos. Chem. Phys., 13, 8833–8855, doi:10.5194/acp-13-8833-2013, 2013.

Stolzenburg, M.: An Ultrafine Aerosol Size Distribution Measuring System, PhD. thesis, Mechanical Engineering Department, University of Minnesota, USA, 1988.

Tarvainen, V., Hakola, H., Hellén, H., Bäck, J., Hari, P and Kulmala, M: Temperature and light dependence of the VOC emissions of Scots pine, Atmos. Chem. Phys., 5, 989–998 doi: 1680-7324/acp/2005-5-989, 2005.

Tunved, P., Hansson, H.-C., Kulmala, M., Aalto, P., Viisanen, Y., Karlsson, H., Kristensson, A., Swietlicki, E., Dal Maso, M., Ström, J., and Komppula, M.: One year boundary layer aerosol size distribution data from five nordic background stations, Atmos. Chem. Phys., 3, 2183–2205, doi:10.5194/acp-3-2183-2003, 2003.

Tunved, P., Hansson, H.-C., Kerminen, V.-M., Ström, J., Dal Maso, M., Lihavainen, H., Viisanen, Y., Aalto, P. P., Komppula, M., and Kulmala, M.: High natural aerosol loading over boreal forests, Science, 312, 261–263, 2006.

Tunved, P., Ström, J., and Krejci, R.: Arctic aerosol life cycle: linking aerosol size distributions observed between 2000 and 2010 with air mass transport and precipitation at Zeppelin station, Ny-Ålesund, Svalbard, Atmos. Chem. Phys., 13, 3643–3660, doi:10.5194/acp-13-3643-2013, 2013.

Uttal, T., Makshtas, A. and Laurila, T.: The Tiksi International Hydrometeorological Observatory – An Arctic Members Partnership, WMO Bulletin 62(1), p.22–26, 2013.

Viskari, T., Asmi, E., Virkkula, A., Kolmonen, P., Petäjä, T., and Järvinen, H.: Estimation of aerosol particle number distribution with Kalman Filtering – Part 2: Simultaneous use of DMPS, APS and nephelometer measurements, Atmos. Chem. Phys., 12, 11781–11793, 2012.

Väänänen, R., Kyrö, E.-M., Nieminen, T., Kivekäs, N., Junninen, H., Virkkula, A., Dal Maso, M., Lihavainen, H., Viisanen, Y., Svenningsson, B., Holst, T., Arneth, A., Aalto, P. P., Kulmala, M., and Kerminen, V.-M.: Analysis of particle size distribution changes between three measurement sites in northern Scandinavia, Atmos. Chem. Phys., 13, 11887–11903, doi:10.5194/acp-13-11887-2013, 2013.

Walsh, J. E., and Chapman, W. L.: Arctic cloud-radiation-temperature associations in observational data and atmospheric reanalysis, J. Climate, 11, 3030–3045, 1998.

Weller, R., Schmidt, K., Teinilä, K., and Hillamo, R.: Natural new particle formation at the coastal Antarctic site Neumayer, Atmos. Chem. Phys., 15, 11399–11410, doi:10.5194/acp-15-11399-2015, 2015.

Wiedensohler, A.: Die bipolare Diffusionsaufladung von Partikeln in chemisch trägen Reinstgasen, PhD thesis, University of Duisburg, Germany, 1989.

Wiedensohler, A., Birmili, W., Nowak, A., Sonntag, A., Weinhold, K., Merkel, M., Wehner, B., Tuch, T., Pfeifer, S., Fiebig, M., Fjäraa, A. M., Asmi, E., Sellegri, K., Depuy, R., Venzac, H., Villani, P., Laj, P., Aalto, P., Ogren, J. A., Swietlicki, E., Williams, P., Roldin, P., Quincey, P., Hüglin, C., Fierz-Schmidhauser, R., Gysel, M., Weingartner, E., Riccobono, F., Santos, S., Grüning, C., Faloon, K., Beddows, D., Harrison, R., Monahan, C., Jennings, S. G., O'Dowd, C. D., Marinoni, A., Horn, H.-G., Keck, L., Jiang, J., Scheckman, J., McMurry, P. H., Deng, Z., Zhao, C. S., Moerman, M., Henzing, B., de Leeuw, G., Löschau, G., and Bastian, S.: Mobility particle size spectrometers: harmonization of technical standards and data structure to facilitate high quality long-term observations of atmospheric particle number size distributions, Atmos. Meas. Tech., 5, 657-685, doi:10.5194/amt-5-657-2012, 2012.

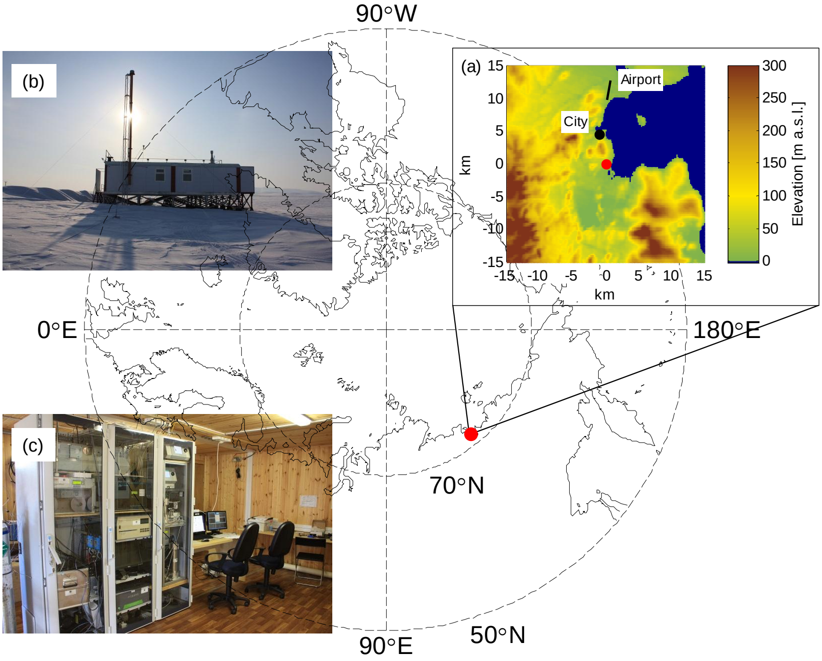
90°W
0°E
180°E
90°E
70°N
50°N
(a)
Airport
City
km
-15
-10
-5
0
5
10
15
Elevation [m a.s.l.]
0
50
100
150
200
250
300
(b)
(c)

Figure 1. Location of the Tiksi measurement station. a) Topographic map insert (United States Geological Survey, 2015[1]) of the surroundings of the measurement site (station indicated by a red dot). b) The station as seen from outside. c) The station interior.

---

[1] United States Geological Survey, Global Multi-resolution Terrain Elevation Data 2010, available at http://earthexplorer.usgs.gov/, last access: 6 May 2015.

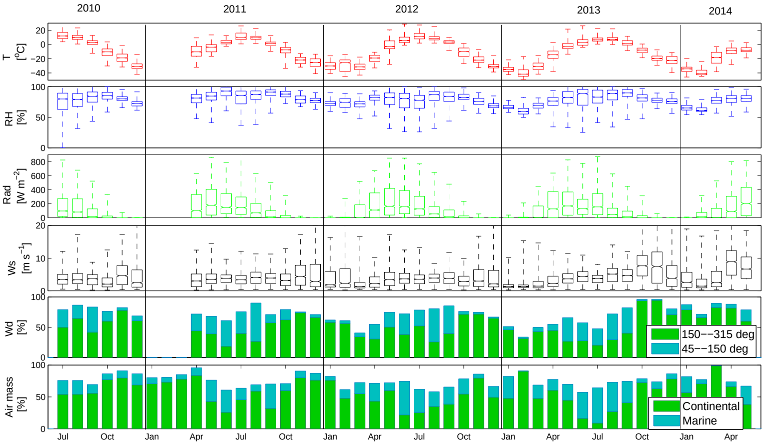

Figure 2. Summary of the meteorological conditions during the measurements. The panels 1–4 (from top to down) depict temperature, relative humidity (RH), global radiation and wind speed, depicted with bars showing extremes, quartiles and median values for each of the parameters monthly. Wind direction (panel 5) is expressed as percents from sector 45–315° (marine sector) and from 150–315° (continental sector), leaving out the sector defined as polluted. Air mass origin (panel 6) is presented as percents of continental (≥70% during preceding 120h) and marine (≥70% during preceding 120h) air masses, leaving out the mixed air masses. Also note that RH is expressed as the ratio of the water vapor pressure to the saturation water vapor pressure over water that is a meteorological convention. In freezing winter conditions, condensation will occur at a lower relative humidity than 100% (over water) when the vapor is saturated against ice.

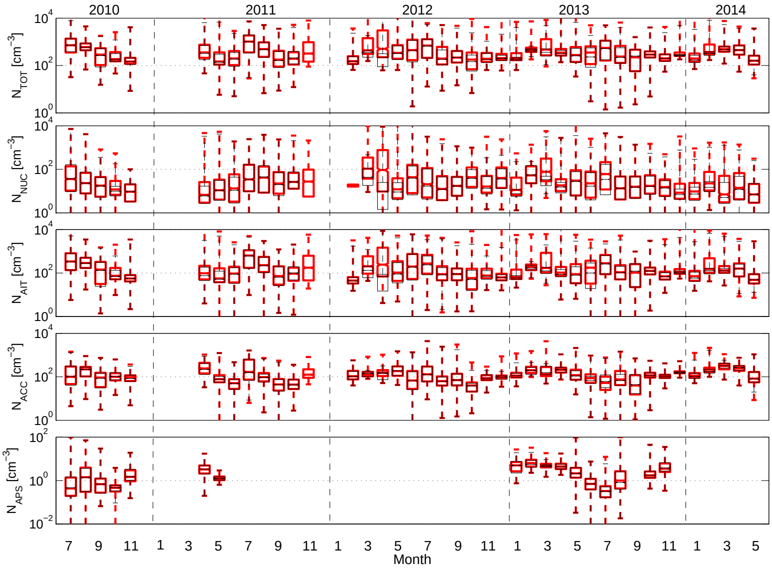

Figure 3. Temporal variability of aerosol total (7–500 nm), nucleation mode (7–25 nm), Aitken mode (25–100 nm), accumulation mode (100–500 nm) and coarse mode (> 410 nm) number concentration, from top to bottom correspondingly. Red bars show quartiles for each month of data available and whiskers the extremes. Black bars are calculated equally but excluding data measured when wind speed was < 2 m s^{-1}. Dotted black lines mark the change of a year.

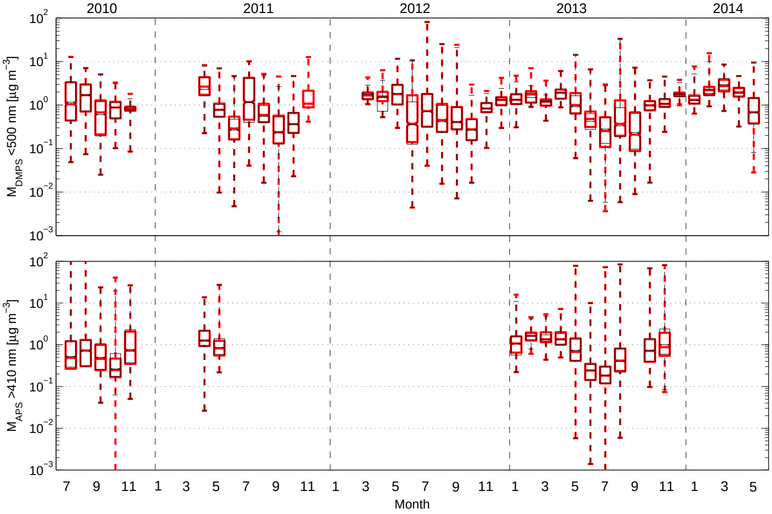

Figure 4. Temporal variability of aerosol total (7–500 nm) and coarse mode (> 410 nm) mass concentration, from top to bottom correspondingly. Red bars show quartiles for each month of data available and whiskers the extremes. Black bars are calculated equally but excluding data measured when wind speed was < 2 m s^{-1}. Dotted black lines mark the change of a year.

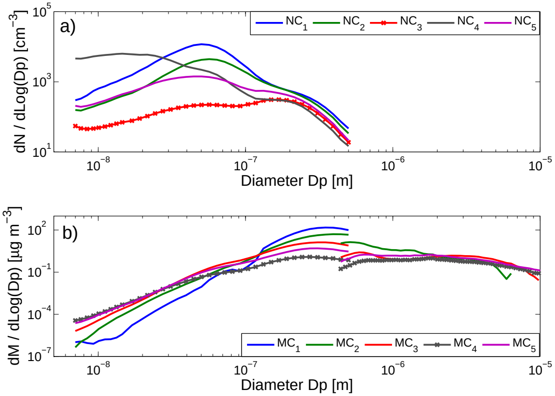

Figure 5. Average particle a) number and b) mass size distributions for different clusters (nro:s 1–5). Crosses mark the most common cluster type found, in both a) and b). In b) the APS mass size distributions (at >410 nm sizes) belonging to each of the clusters are also presented for times when available.

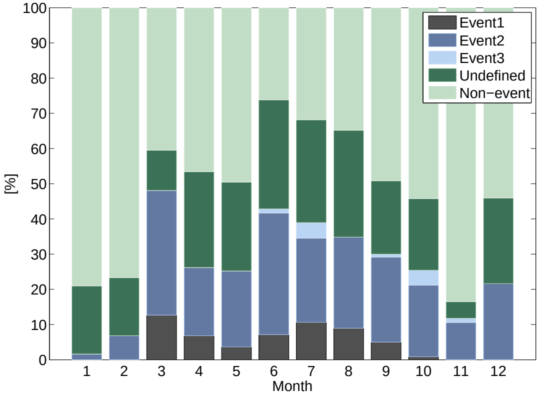

Figure 6. Classification of particle formation events into classes: 1 (strong event), 2 (weaker event but calculation of growth rate (GR) and formation rate (FR) possible), 3 (weak event, not possible to calculate GR and FR), undefined and non-event day. Fractions of different type of events are shown monthly for the whole period of measurements of about four years. More details on classification is found at Dal Maso et al. (2005).

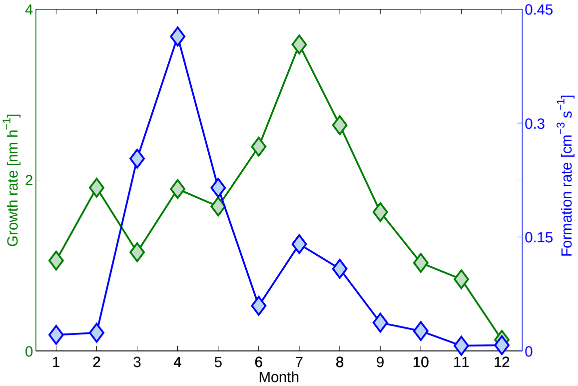

Figure 7. Monthly averages of particle growth rates (green) and formation rates (blue) for all class 1 and class 2 events. Note: particle formation rates were calculated for the lowest observed particle size, which was not however in all cases the lowest measurable size of 7 nm.

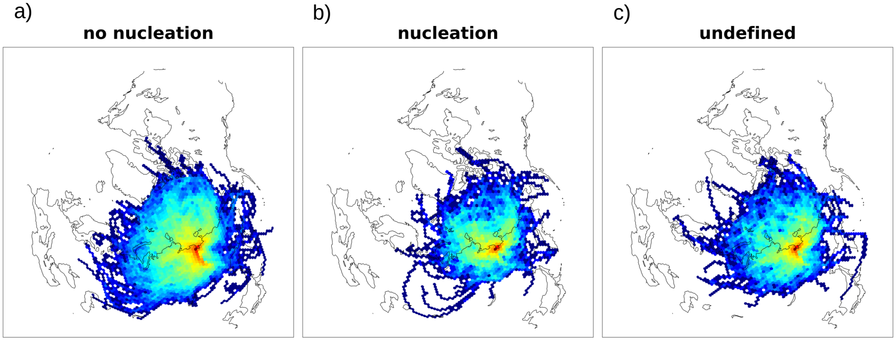

Figure 8. Back trajectories for air masses in non-event days (a), at the start of the NPF events (b), and at 11am local time in undefined days (c). Figures a), b), and c) consist of 551, 259 and 244 individual trajectories, respectively. The trajectories were calculated using HYSPLIT 4 (Draxler and Hess, 1998) with an arrival height of 500 meters above ground level calculated 120 hours backwards in time. The color coding of the figure represents the number of trajectories that have passed over a geodesic hexagon on the map. Each trajectory coordinate was associated with a specific hexagon according to the minimum distance of a trajectory coordinate to the centroid of the grid cell. Trajectories residing over a grid cell is calculated once in order to circumvent weighing due to residence time over grid cells. The color coding of the figure is logarithmic with red depicting frequently passed grid cells while the cooler colors represents infrequent trajectory overpasses.

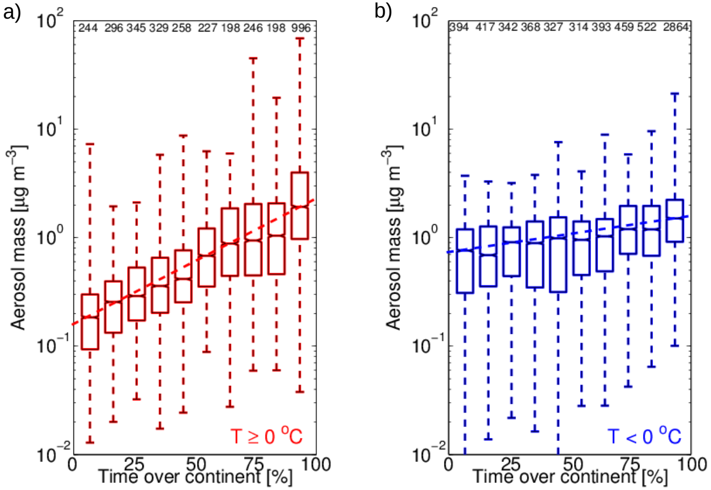

Figure 9. Aerosol total mass ($\leq$ 500 nm) versus percentage of time the air mass spent over continental areas over the last 120 hours. Median mass concentration around each back-trajectory (for every 3h) was used in calculations. In left panel (a) in red are depicted the data measured in temperatures $\geq$0 °C and in right panel (b) those in temperatures <0 °C. Boxes show the quartiles with whiskers extending to extreme data points. On top of each box is the number of cases used in calculations. Dash red and blue lines are added to guide the eye.

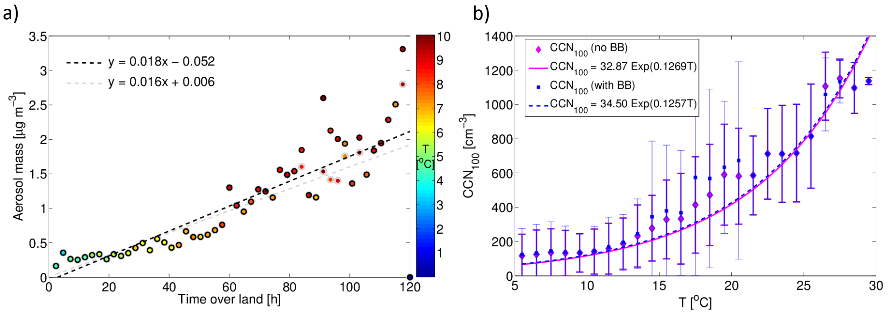

Figure 10. a) Average aerosol total mass ($\leq$ 500 nm) as a function of air mass time spent over land. Circles with grey borders present all data and circles with black borders data without significant BB influence (i.e. data belonging to mass clusters indicative of biomass burning are not used; for reference, see Figure 5b). Colors inside circles indicate the average temperature for each point. Dashed grey and black line show the linear fits (R_2=0.84 for all data; R_2=0.88 for no BB) to data points along with the fitting equations obtained. b) Average CCN_{100} concentration calculated from all data (blue squares) and from data without significant BB influence (purple diamonds), plotted as a function of outdoor air temperature with a exponential fits to the data (R_2=0.97 for all data; R_2=0.98 for no BB). Bars around averages present the standard deviation.

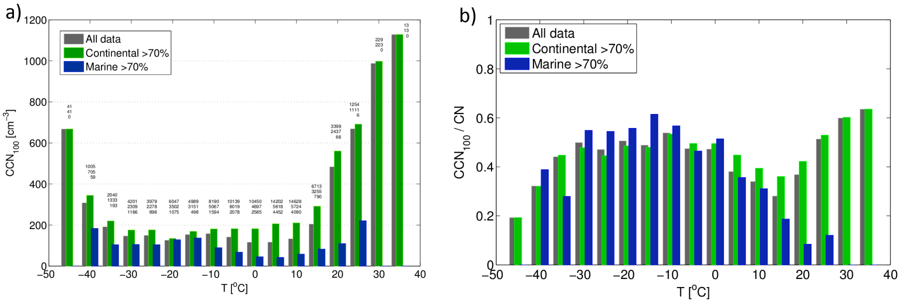

Figure 11. a) Average CCN_{100} concentration as a function of measurement temperature. Different bars present cases calculated using all data (dark grey), continental data (green) and marine data (blue). The numbers on top of each bar show the amount of DMPS data available for each total, continental and marine cases, from top to down, which is equal also for figure b). b) Average CCN_{100} to CN ratio as a function of measurement temperature. Different bars present cases calculated using all data (dark grey), continental data (green) and marine data (blue).

Table 1. Average and median number and mass concentrations for different months. First column indicate the month and second column (N) the amount of data used in averaging for DMPS and APS instruments. The following columns present monthly average ($\bar{N}_{TO}$, $\bar{N}_{NU}$, $\bar{N}_{AI}$, $\bar{N}_{AC}$, $\bar{N}_{CO}$, $\bar{M}_{TO}$, $\bar{M}_{CO}$) and median ($\tilde{N}_{TO}$, $\tilde{N}_{NU}$, $\tilde{N}_{AI}$, $\tilde{N}_{AC}$, $\tilde{N}_{CO}$, $\tilde{M}_{TO}$, $\tilde{M}_{CO}$) values calculated for total (7–500 nm), nucleation mode (7–25 nm), Aitken mode (25–100 nm), accumulation mode (100–500 nm) and coarse mode ($>$ 410 nm) number and for DMPS and APS total mass, respectively.

Month	N (DMPS/APS) [cases]	$\bar{N}_{TO}$ ($\tilde{N}_{TO}$) [cm^{-3}]	$\bar{N}_{NU}$ ($\tilde{N}_{NU}$) [cm^{-3}]	$\bar{N}_{AI}$ ($\tilde{N}_{AI}$) [cm^{-3}]	$\bar{N}_{AC}$ ($\tilde{N}_{AC}$) [cm^{-3}]	$\bar{N}_{CO}$ ($\tilde{N}_{CO}$) [cm^{-3}]	$\bar{M}_{TO}$ ($\tilde{M}_{TO}$) [μg m^{-3}]	$\bar{M}_{CO}$ ($\tilde{M}_{CO}$) [μg m^{-3}]
1	4534/1734	469 (200)	36 (10)	297 (69)	139 (112)	5.3 (5.0)	1.38 (1.24)	1.60 (1.07)
2	4070/1680	639 (329)	83 (27)	370 (119)	222 (182)	7.4 (6.3)	2.03 (1.72)	1.72 (1.64)
3	4825/2472	762 (481)	146 (19)	358 (140)	276 (267)	5.0 (4.8)	2.60 (2.38)	1.69 (1.36)
4	7470/7512	725 (396)	130 (14)	341 (123)	258 (222)	4.3 (4.0)	2.18 (1.89)	1.74 (1.31)
5	9903/6028	529 (222)	89 (12)	259 (69)	185 (113)	3.5 (1.8)	1.59 (0.96)	1.18 (0.70)
6	7776/4656	620 (327)	142 (26)	338 (147)	144 (71)	1.2 (0.7)	0.95 (0.42)	0.34 (0.24)
7	10701/9267	970 (724)	172 (35)	567 (343)	241 (102)	1.0 (0.4)	1.94 (0.60)	1.01 (0.32)
8	11570/9572	590 (383)	111 (19)	322 (161)	160 (90)	4.3 (1.1)	1.41 (0.56)	1.15(0.48)
9	12651/6606	324 (222)	61 (18)	160 (98)	105 (60)	1.0 (0.7)	0.83 (0.36)	0.74 (0.46)
10	11950/7627	302 (227)	64 (21)	150 (98)	90 (76)	1.5 (1.1)	0.70 (0.57)	1.39 (0.45)
11	8534/9910	280 (184)	38 (15)	143 (68)	106 (98)	4.0 (3.1)	1.04 (0.94)	1.70 (0.83)
12	2891/0	415 (253)	71 (23)	220 (84)	126 (116)	–	1.35 (1.33)	–

Table 2. Total particle number concentration (N), temperature (T), RH, solar radiation (Rad), wind speed (Ws), percentage over continental areas (Cont), and black carbon mass concentration (uncorrected) (BC) for different size distribution clusters (numbers 1–5, referring to Fig. 5a). Number of cases available for each cluster is shown in parenthesis below the cluster number. For different variables both average (upper row) and median (lower row) are calculated, and for total number also standard deviation is presented.

Cluster nro (cases)	N [$\mathrm{cm^{-3}}$]	T [°C]	RH [%]	Rad [$\mathrm{W\,m^{-2}}$]	Ws [$\mathrm{m\,s^{-1}}$]	Cont [%]	BC [$\mathrm{ng\,m^{-3}}$]
1	5967 ± 2237	–18.2	69	136	2.1	75	360
(70)	5272	–25.6	67	16	1.4	84	327
2	2490 ± 749	–3.7	67	181	2.8	77	214
(536)	2360	8.9	67	80	1.8	86	145
3	301 ± 243	–5.9	80	106	5.0	63	127
(10187)	240	–3.4	81	22	4.3	69	44
4	4941 ± 2699	–5.6	70	402	2.7	51	123
(84)	4214	2.5	71	410	2.5	43	86
5	1193 ± 443	0.6	73	171	3.5	70	119
(1758)	1104	6.6	76	88	2.9	75	46

Table 3. Total particle mass concentration from DMPS data (M), from APS data (M_{APS}), temperature (T), RH, solar radiation (Rad), wind speed (Ws), percentage over continental areas (Cont), and black carbon mass concentration (uncorrected) (BC) for different size distribution clusters (numbers 1–5, referring to Fig. 5b). Number of cases available for each cluster is shown in parenthesis below the cluster number, and the number of cases from APS after this. For different variables both average (upper row) and median (lower row) are calculated, and for total number also standard deviation is presented.

Cluster nro (cases/APS)	M [μg m^{-3}]	M_{APS} [μg m^{-3}]	T [°C]	RH [%]	Rad [W m^{-2}]	Ws [m s^{-1}]	Cont [%]	BC [ng m^{-3}]
1	52.1 ± 10.7	–	17.0	81	14	4.4	95	1674
(11/0)	47.4	–	17.6	84	10	4.8	100	1551
2	18.4 ± 4.0	7.8 ± 0.6	15.1	76	136	3.5	93	734
(43/16)	19.2	7.8	17.0	85	68	3.2	100	745
3	5.8 ± 1.7	1.7 ± 1.3	6.5	70	176	4.8	93	207
(676/269)	5.3	1.4	7.8	74	100	4.4	100	135
4	0.6 ± 0.4	0.8 ± 1.4	–3.8	81	115	4.6	55	75
(8438/3001)	0.5	0.4	–0.5	82	30	4.0	50	21
5	2.3 ± 0.7	1.6 ± 2.1	–10.6	74	122	4.8	81	233
(3467/1009)	2.1	1.1	–9.5	74	20	3.7	98	132

Table 4. Secondary particle growth rates and formation rates in different months. First column indicate the month. Second column (GR) and third column (FR_7) show the particle growth rate and formation rate parameters calculated for class1 events only. Forth column (GR_{ALL}) and fifth column (FR_{ALL}) present the growth rate and formation rate parameters calculated for all the events (class2 included). Values in each column present the monthly averages with standard deviations followed by the medians in parenthesis.

Month	$\bar{GR} \pm$ STD ($\tilde{GR}$) [nm h^{-1}]	$\bar{FR_7} \pm$ STD ($\tilde{FR_7}$) [cm^{-3} s^{-1}]	$\bar{GR}_{ALL} \pm$ STD ($\tilde{GR}_{ALL}$) [nm h^{-1}]	$\bar{FR}_{ALL} \pm$ STD ($\tilde{FR}_{ALL}$) [cm^{-3} s^{-1}]
1	–	–	1.1 ± 0.0 (1.1)	0.02 ± 0.00 (0.02)
2	–	–	1.9 ± 1.1 (2.6)	0.02 ± 0.01 (0.03)
3	1.5 ± 0.3 (1.4)	0.40 ± 0.32 (0.22)	1.2 ± 0.7 (1.0)	0.25 ± 0.24 (0.19)
4	3.2 ± 1.1 (2.6)	0.46 ± 0.25 (0.35)	1.9 ± 1.3 (2.0)	0.41 ± 0.54 (0.26)
5	3.3 ± 0.8 (3.4)	0.90 ± 0.50 (0.89)	1.7 ± 1.5 (1.1)	0.21 ± 0.42 (0.01)
6	3.8 ± 1.6 (3.9)	0.19 ± 0.11 (0.17)	2.4 ± 2.0 (1.7)	0.06 ± 0.08 (0.03)
7	4.8 ± 2.7 (3.9)	0.30 ± 0.24 (0.19)	3.6 ± 2.5 (3.1)	0.14 ± 0.18 (0.09)
8	3.6 ± 1.8 (3.1)	0.19 ± 0.13 (0.18)	2.6 ± 1.7 (2.4)	0.11 ± 0.17 (0.05)
9	4.0 ± 1.6 (4.5)	0.10 ± 0.07 (0.09)	1.6 ± 1.5 (1.1)	0.04 ± 0.05 (0.01)
10	3.6 ± 0.0 (3.6)	0.06 ± 0.00 (0.06)	1.0 ± 1.0 (0.8)	0.03 ± 0.04 (0.01)
11	–	–	0.8 ± 0.4 (1.0)	0.01 ± 0.01 (0.01)
12	–	–	0.1 ± 0.2 (0.0)	0.01 ± 0.00 (0.01)